We are IntechOpen, the world's leading publisher of Open Access books Built by scientists, for scientists

6,900
Open access books available

186,000
International authors and editors

200M
Downloads

Our authors are among the

154
Countries delivered to

TOP 1%
most cited scientists

12.2%
Contributors from top 500 universities

CLARIVATE ANALYTICS
BOOK CITATION INDEX
INDEXED

WEB OF SCIENCE™

Selection of our books indexed in the Book Citation Index
in Web of Science™ Core Collection (BKCI)

Interested in publishing with us?
Contact book.department@intechopen.com

Dental Materials

Junko Hieda, Mitsuo Niinomi, Masaaki Nakai and Ken Cho

Additional information is available at the end of the chapter

http://dx.doi.org/10.5772/55049

1. Introduction

Metallic biomaterials used for dental applications, which are called dental alloys, and such alloys require a high corrosion resistance because the pH and temperature vary widely in the oral environment where foods and beverages are taken in. These alloys also require biocompatibility in order to prevent an allergic reaction to the metals. Dental alloys are mainly used to make devices for filling cavities and as substitutes for teeth that are lost because of decay and periodontal disease. A variety of dental devices have been developed, which include metallic fillers, inlays, crowns, bridges, clasps, dentures, dental implants composed of a fixture and an abutment, and fixed braces (train tracks). These forms of dental restoration, custom-shaped for an individual, are made by casting; therefore, the castability of alloys is another requirement for dental applications.

Dental alloys are mainly classified into two groups: precious and nonprecious metals. Suitable alloys are employed according to the intended use. Alloys of precious metals such as gold (Au), palladium (Pd), and silver (Ag) are usually employed because of their high corrosion resistance, biocompatibility, and castability, as compared to those of nonprecious metals. Precious alloys are grouped into high-carat alloy (high-precious or -nobility alloy) and low-carat alloy (low-precious or –nobility alloy). The high-carat alloy contains more than 75 % precious metals. Non-precious metal alloys such as stainless steels, cobalt-chromium, nickel-chromium, and titanium alloys are also commonly used.

Among the dental alloys, precious alloys are widely used. Au alloys have been commonly used in dental applications from past to the present, and many commercial variations of alloy compositions have been developed, despite their high cost. American Dental Association classifies these Au alloys on the basis of their mechanical properties. Many studies have been carried out to improve the mechanical properties of the Au alloys containing copper (Cu) (Au–Cu–Pd [1, 2], Au–Ag–Pd–In [3], Au–Cu–Zn [4], Au–Cu–Zn–Ag [5], and Au–Ag–Cu–Pd [6]

alloys), with the main focus on the microstructural changes produced by heat treatment. However, recent trends have shown that low-carat dental alloys (Ag and Pd alloys) are attracting much attention as alternatives to Au alloys because of their lower price. Thus, Ag alloys such as Ag–Pd–Cu–Au [7-17], and Ag–Cu–Pd–Au [18, 19] alloys have been developed for commercial applications. The hardness of these alloys increases with aging or solution treatment, and many studies have reported on the behaviors of these alloys in response to various heat treatments and the various mechanisms. Dental casting of Ag–20Pd–14.5Cu-12Au alloy (mass%) has been developed and used widely in Japan. In general, this alloy is subjected to aging treatment (AT) at around 673 K after solution treatment (ST) at 1023 K in order to enhance its mechanical strength. Recently, it has been reported that the mechanical strength of Ag–20Pd–14.5Cu–12Au alloy is significantly enhanced when the alloy is subjected to ST at temperatures higher than 1073 K and subsequently water quenched without any AT [9-16]. The Vickers hardness of this alloy increases with an increase in the cooling rate after ST [11]. This unique hardening behavior and the increase in mechanical strength induced by the high-temperature ST have been explained in terms of the precipitation hardening caused by the precipitation of an $L1_0$-type ordered β' phase.

This chapter describes with focusing on the relationship between the unique hardening behavior exhibited by the as-solutionized dental Ag–Pd–Cu–Au alloys and the corresponding microstructural changes. Other mechanical properties (fatigue, fretting-fatigue, and friction wear properties) and corrosion properties are also described.

## 2. Age hardening behavior of Ag–Pd–Cu–Au alloys

Ag-Pd alloys have complete miscibility in all composition ratios. Addition of Cu leads to age hardening in these alloys. In the early researches during 1960–70s, mechanisms for age hardening of Ag-Pd-Cu alloys were proposed [20-22]. According to them, the age hardening was caused by the formation of a CuPd ordered phase ($L2_0$-type) [20], precipitation of a Cu-rich α_1 phase [21], and phase separation of α solid solution to a CuPd ordered phase ($L2_0$-type) and Ag-rich α_2 phase [22]. More recently, Au has been added to Ag-Pd-Cu alloys to increase their corrosion resistance. Therefore, since 1980 to the present, many studies have focused on the age-hardening mechanism of the Ag-Pd-Cu-Au alloys (Table 1) [8, 19, 23, 24]. Ohta et al. [23] reported that the precipitation of a $L1_0$-type face-centered tetragonal CuPd ordered platelet (β') inside the grains and discontinuous precipitation of the Ag-rich α_2 phase and CuPd ordered phase (β) in the grain boundary regions enhance the hardening of Ag-Pd-Cu-Au alloys with a low Au content (Au = 10 mass%). According to their report, TEM images of the precipitates (β and α_2) along the grain boundaries in the alloys show strain contrast and moiré fringes, which indicates that β and α_2 phases are coherent with each other. Solution hardening behavior was also found in alloys subjected to ST at 1223 K followed by slow quenching (SQ) before aging. Researches since 2000 have focused on the age hardening behavior of the Ag-Pd-Cu-Au alloys as a function of the treatment duration [8, 19]. It was found that during the early stage of the aging, diffusion and aggregation of Cu atoms from the Ag-rich α phase occur, and

in the later stage, the hardness of the alloy decreases because of the coarsening of the Cu-rich lamellar precipitates [8, 19]. At a Cu concentration of 20 mass%, the CuPd ordered phase (β) does not exhibit any change after aging and thus does not contribute to the age hardening [19].

The age-hardening mechanism of Ag-Pd-Cu-Au alloys with an Au content of 20 mass% was also investigated, and it was concluded that β' and the discontinuous Ag-rich α_2 phase contribute to the age hardening of these alloys [24]. Fig.1 shows the hardness (Hv) of the precipitates measured independently inside the grains (inter grain) and along the grain boundaries (nodule) [24]. These curves indicate that there are two hardening stages of the alloys in terms of aging temperature: the formation of β' phase in the grain interior at low aging temperatures and the precipitation of the Ag-rich α_2 phase along the grain boundaries at high aging temperatures. It was also found that the Cu concentration influences the formation of β' phase in these alloys (Fig. 2) [24]. The hardness (H_v) of each alloy increases with an increase of the Cu concentration, i.e. the volume fraction of β' phase, at any temperatures.

| Compositions of Ag-Pd-Cu-Au alloys (mass%)	References
Ag-20.9Pd-8.5Cu-12.5Au-2.5Zn-0.5Sn-0.1Ir	[8]
Ag-20Pd-20Cu-12Au-2(Zn, Ir, and In)	[19]
Ag-25.4Pd-21.8Cu-10Au	[23]
Ag-25.20Pd-9.88Cu-20Au, Ag-30.32Pd-9.66Cu-5.04Au, Ag-25.4Pd-12.82Cu-9.96Au, Ag-28Pd-9.12Cu-12.04Au	[24]

Table 1. Compositions of Ag-Pd-Cu-Au alloys (mass%).
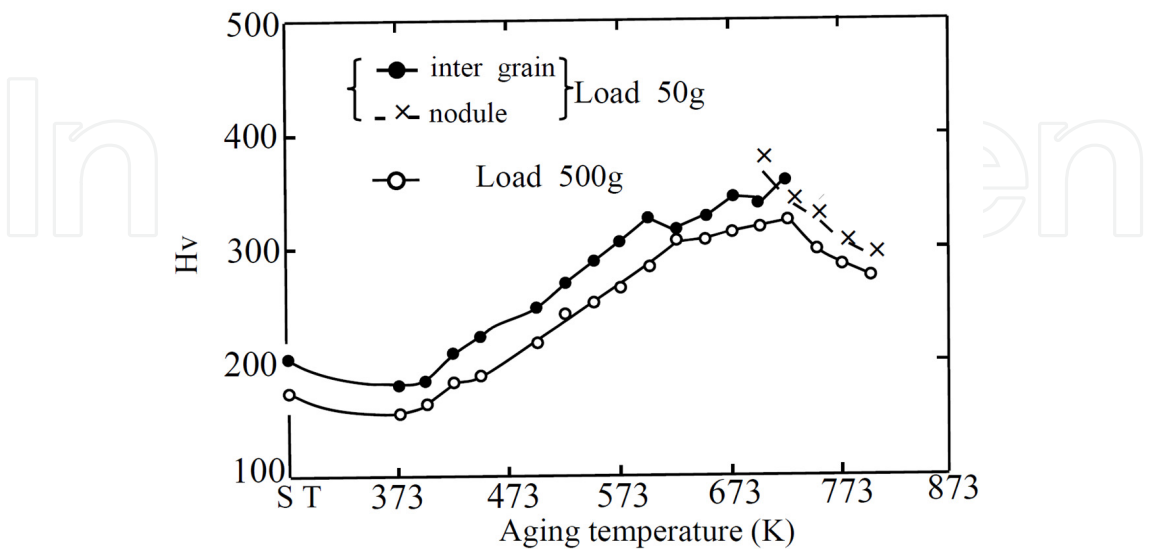
Figure 1. Anisothermal age hardening curve of Ag-25.2Pd-9.88Cu-20Au alloy.
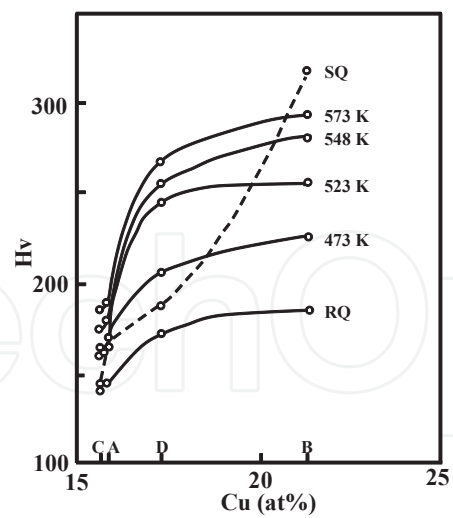
Figure 2. Effect of Cu concentration (at%) on hardness (Hv) of Ag-30.32Pd-9.66Cu-5.04Au (A), Ag-25.4Pd-12.82Cu-9.96Au (B), Ag-28Pd-9.12Cu-12.04Au (C), and Ag-25.2Pd-9.88Cu-20Au (D) alloys. SQ and RQ indicate specimens subjected to slow quenching and rapid quenching after ST, respectively.
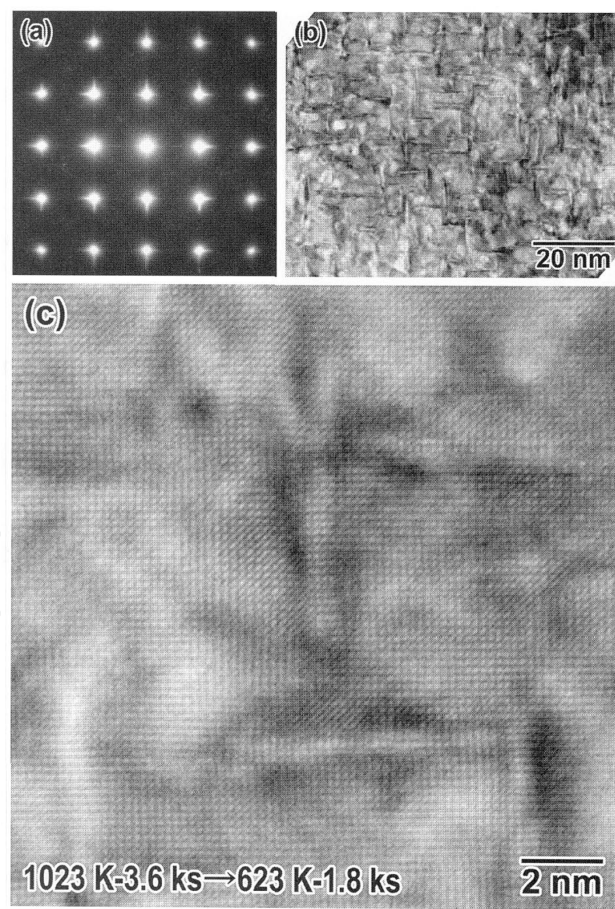
Figure 3. (a) Diffraction pattern, (b) TEM image, and (c) HRTEM image of Ag-Pd-Cu-Au alloy subjected to ST at 1023 K for 3.6 ks followed by aging treatment at 623 K for 1.8 ks.

Figure 3 shows a diffraction pattern, a transmission electron microscopy (TEM) image, and a high resolution TEM (HRTEM) image of β' phase formed in the Ag–20Pd–14.5Cu–12Au alloy subjected to ST at 1023 K for 3.6 ks followed by AT at 623 K for 1.8 ks [25]. β' phase is platelet shape with the size of about 10 nm long, which precipitates parallel to {200} crystal plane of matrix. A lattice constant of a-axis matches with that of the matrix, which exhibits coherent with the matrix [25].
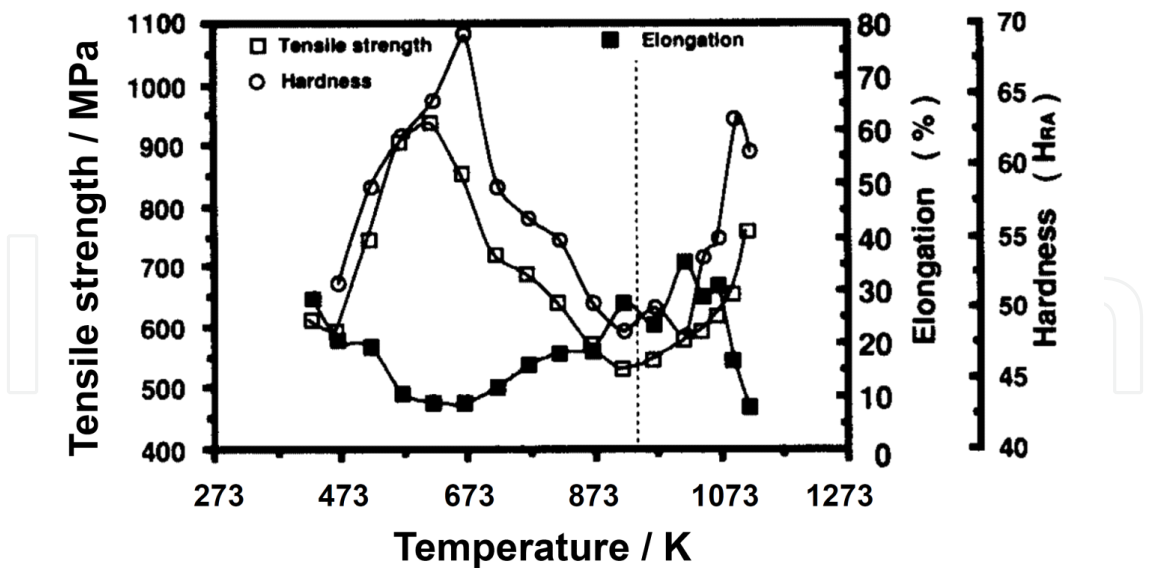
3. Mechanical properties of Ag–20Pd–14.5Cu–12Au alloy

3.1. Unique hardening behavior

3.1.1. Precipitation of β' phase after high temperature solution treatment

Commercial Ag–20Pd–14.5Cu–12Au dental alloy (as-received) is fabricated by a rolling process. The commercial Ag–20Pd–14.5Cu–12Au alloy has a multiphase microstructure (α_1, α_2, β). It is well known that the Ag–Pd–Cu–Au alloy exhibits age hardening behavior as described in the section 2, but the drastic increase in the hardness of Ag–20Pd–14.5Cu–12Au alloy through ST at temperatures over 1073 K subjected to water quenching has been newly reported [10]. This unique hardening behavior has been explained in terms of two hardening mechanisms: (1) solid solution hardening mechanism in which the alloying elements are dissolved into the matrix (α phase) during ST, and (2) precipitation hardening mechanism, in which $L1_0$-type ordered phases are precipitated during the quenching process after ST. Recent studies on the hardening mechanism of Ag–20Pd–14.5Cu–12Au alloy have revealed that the precipitation hardening mechanism is the probable mechanism for the unique hardening behavior exhibited [11, 26].

Conventionally, dentists have employed AT for the hardening of Ag–20Pd–14.5Cu–12Au alloy as mentioned above. Figure 4 [10] shows the effects of heat treatment (AT and ST) temperatures on the mechanical properties (tensile strength, elongation, and hardness (H_{RA})) of this alloy. The tensile strength and hardness increase until the temperature reaches 673 K, and then decrease for up to 923 K due to the removal of strain from the alloy. At temperatures higher than 923 K, this alloy exhibits a unique hardening behavior. Under AT, the tensile strength and hardness of this alloy drastically increase and the elongation decreases after treatment at 673 K. On the other hand, under ST, the tensile strength and hardness still increase but the elongation does not decrease after treatment at 1073 K. Since high temperature ST is very useful for the hardening of this alloy, this treatment will be widely adopted in the future.

The relationship between the microstructural changes in the $L1_0$-type ordered β' phase and the hardening behavior in the solutionized alloys was investigated by changing the cooling rate. Figure 5 shows a schematic drawing of various cooling rates employed after ST [11]. The Vickers hardness of the as-received alloy and of the alloys subjected to ST followed by water quenching (WQ), air cooling (AC), and cooling in a furnace (FC) are shown in Fig. 6 [11]. ST subjected to WQ and AC leads to a significant and slight increase in the hardness of the alloy,

Figure 4. Effect of heat treatment temperature on mechanical properties of Ag–20Pd–14.5Cu–12Au alloy.

respectively, while ST subjected to FC decreases the hardness of the alloy. Thus, the hardness tends to decrease with a decrease in the cooling rate after ST.

Figures 7 and 8 show the microstructures of the as-received and solutionized alloy, respectively, as measured by backscattered electron (BSE) and energy dispersive X-ray spectroscopy (EDX) analysis [13]. The as-received alloy composed of a Cu-rich α_1 phase, an Ag-rich α_2 phase, and Cu–Pd intermetallic β phase, while the solutionized alloy composed of α_2 and β phases. After ST, the α_1 phase dissolved into the Ag-rich α_2 phase and the β phase remained in the matrix. The β' phase precipitated in the matrix could not be observed by BSE, but could be observed by TEM.
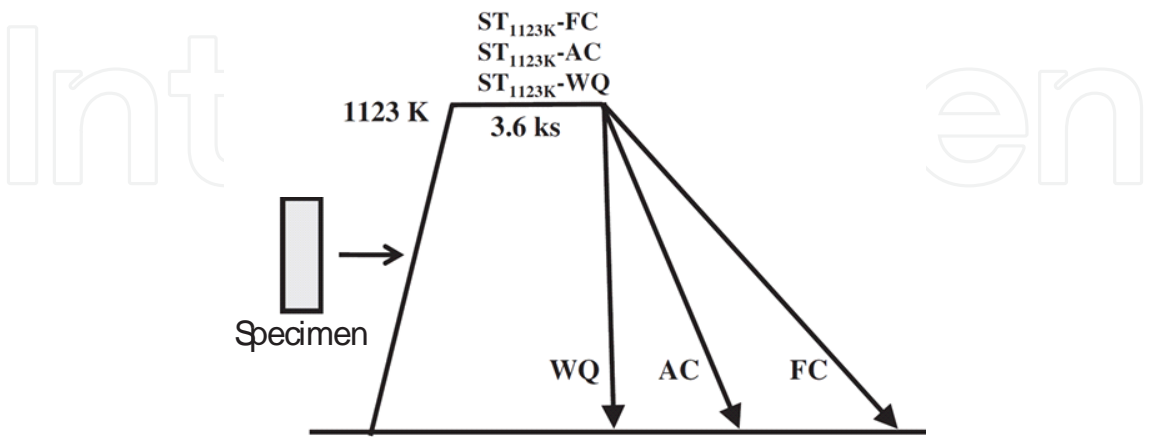
Figure 5. Schematic drawing of heat treatments with various cooling rates after ST. ST_{1123K}-WQ, ST_{1123K}-AC, and ST_{1123K}-FC indicate specimens subjected to ST at 1123 K followed by water, air, and furnace cooling, respectively.
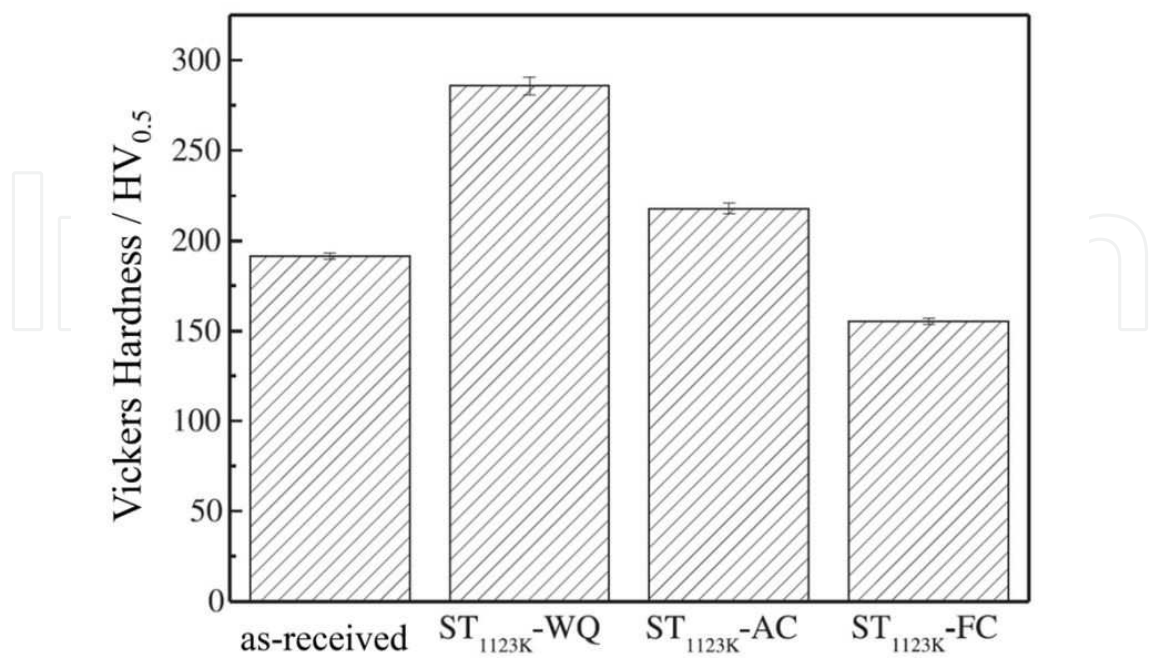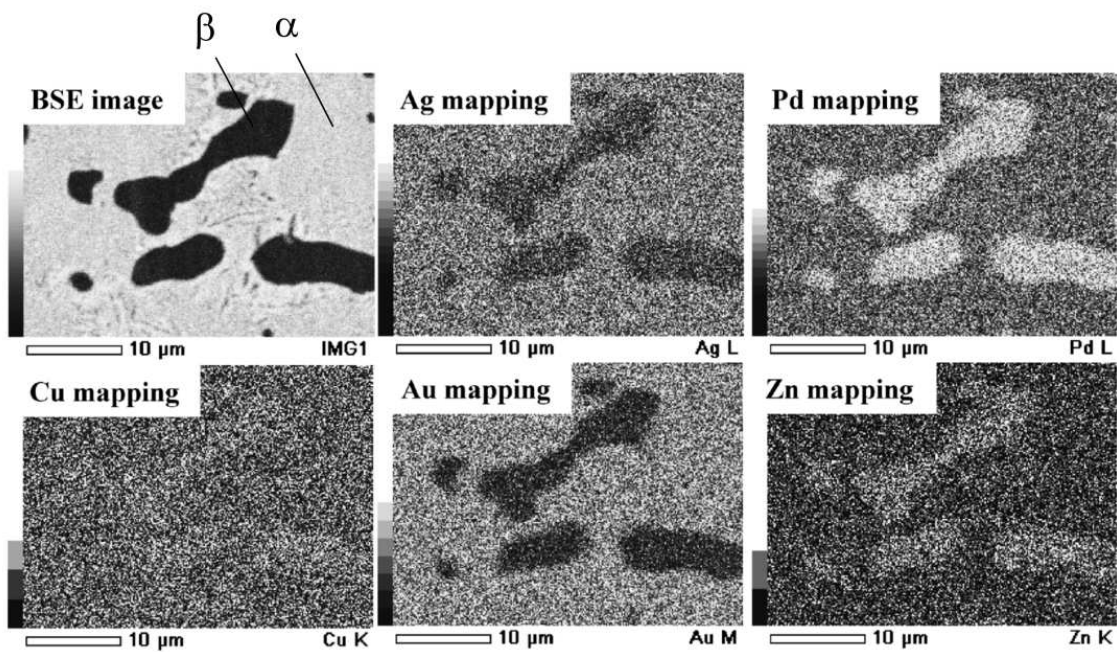
Figure 6. Vickers hardness of as-received, ST$_{1123K}$-WQ, ST$_{1123K}$-AC, and ST$_{1123K}$-FC.
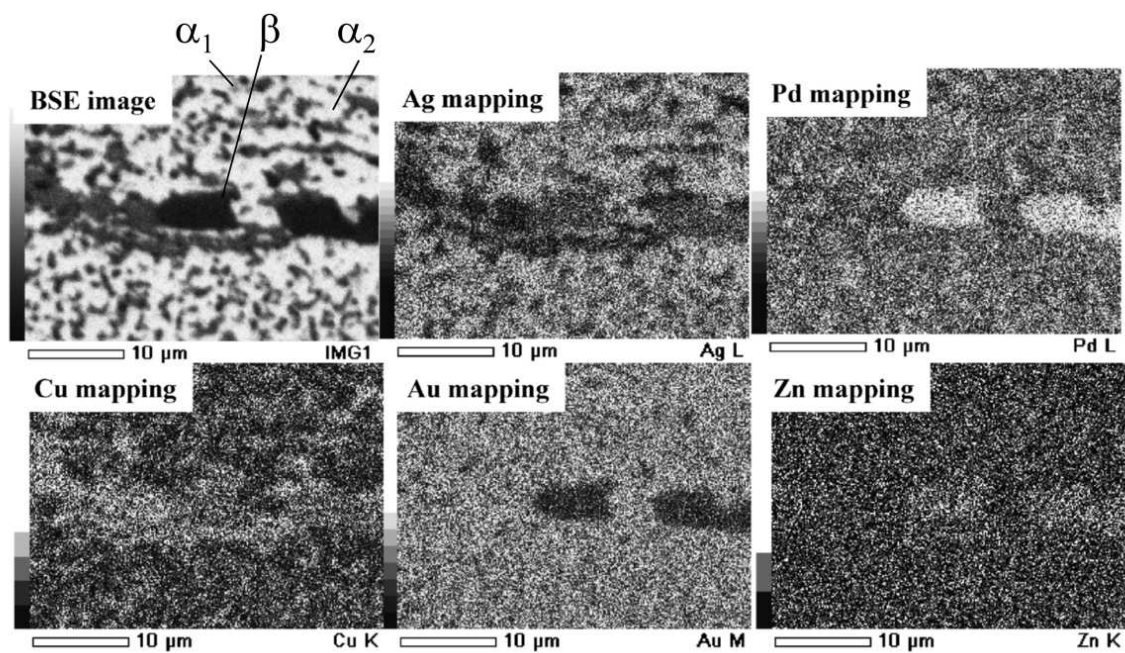

Figure 7. BSE image and elemental mappings obtained by EDX of as-received Ag–20Pd–14.5Cu–12Au alloy.

Figure 8. BSE image and elemental mappings obtained by EDX of Ag–20Pd–14.5Cu–12Au alloy subjected to ST at 1123 K for 3.6 ks.

The selected area diffraction patterns (SADP) and key diagrams obtained from TEM for the alloy subjected to ST and WQ, given in Fig. 9, show that three variants of the $L1_0$-type ordered β' phase are present when the beam direction is parallel to [100] crystal direction: one variant (P) has a c-axis parallel to the electron beam; the other two variants (N_1, N_2) have c-axes normal to the electron beam [11]. The SADPs indicate that an $L1_0$-type ordered β' phase is densely precipitated in the matrix. The dark field images using a $(001)N_1$ and $(001)N_2$ reflections (Fig. 9 (d) and (e)) show that the β' phase is 2–6 nm wide and 20–60 nm long. In the alloy subjected to ST and AC, the β' phase is 3–13 nm wide and 50–400 nm long, and in the alloy subjected to ST and FC the β' phase is 3–25 nm wide and 70–700 nm long, as confirmed by the dark field images using a $(001)N_1$ reflection. In the alloys subjected to ST followed by AC and FC, the β' phase is less densely precipitated than the alloy subjected to ST and WQ. These dark field images indicate that the size and number of the β' phase vary with the cooling rates after ST. In the solutionized alloy subjected to WQ, the size of the β' phase is small and the amount of the β' phase is large. The size of the β' phase decreased and the amount of the β' phase increased with an increase in the cooling rate after ST. The driving force behind the nucleation of the β' phase in the solutionized alloy subjected to WQ is stronger than that in the solutionized alloy subjected to AC and FC, because the degree of undercooling in the solutionized alloy subjected to WQ is larger than that in the solutionized alloy subjected to AC and FC. The extent of nucleation of the β' phase in the solutionized alloy subjected to WQ is larger than that in the solutionized alloy subjected to AC and FC. The β' phase in the solutionized alloys subjected to AC and FC grew more coarsely than that in the solutionized alloy subjected to WQ, because the diffusion occurred more easily owing to the slow cooling process in the solutionized alloys subjected to AC and FC. Therefore, it is likely that the β' phase is formed during the cooling process and grows by diffusion.
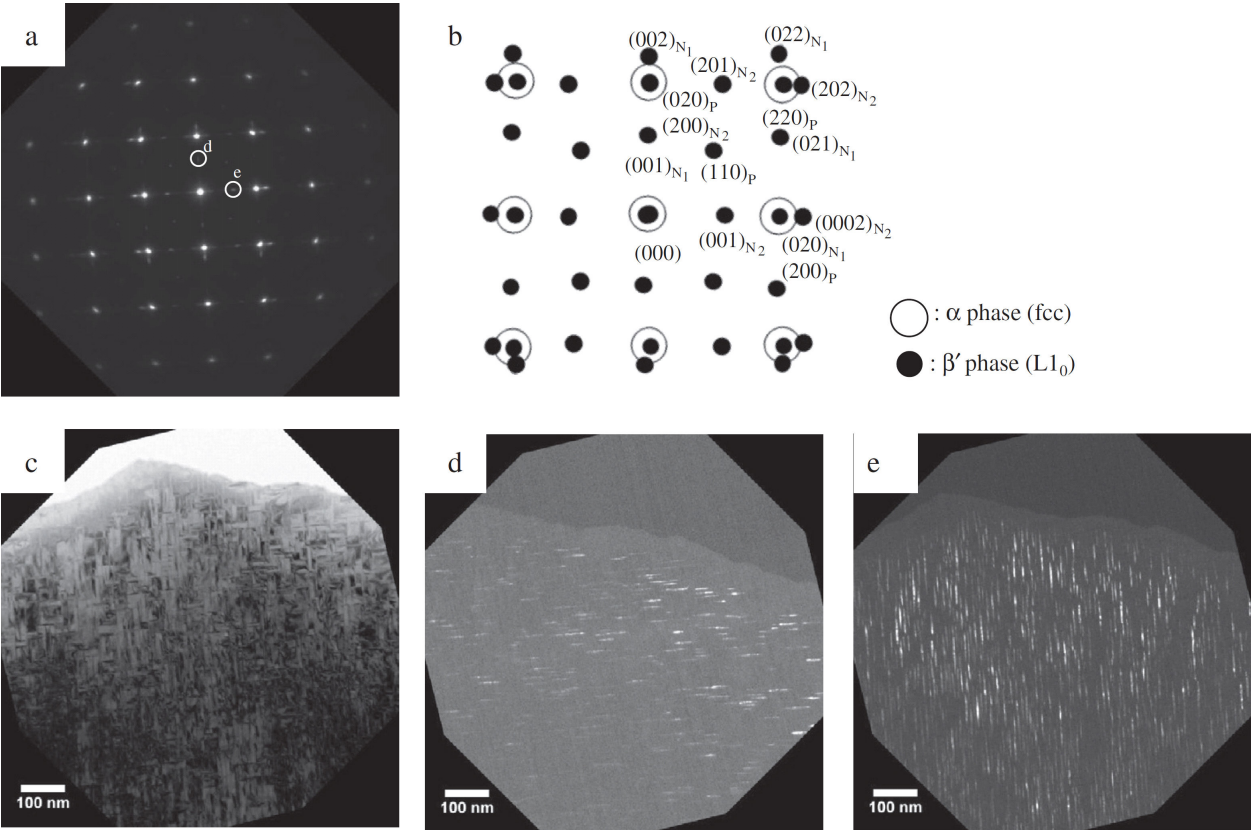
Figure 9. TEM micrographs of ST_{1123K}-WQ: (a) a selected area diffraction pattern, (b) a key diagram, (c) a bright-field image, and (d) and (e) dark-field images using $(001)N_1$ and $(001)N_2$ reflections, respectively. The beam direction is parallel to [100] crystal direction.
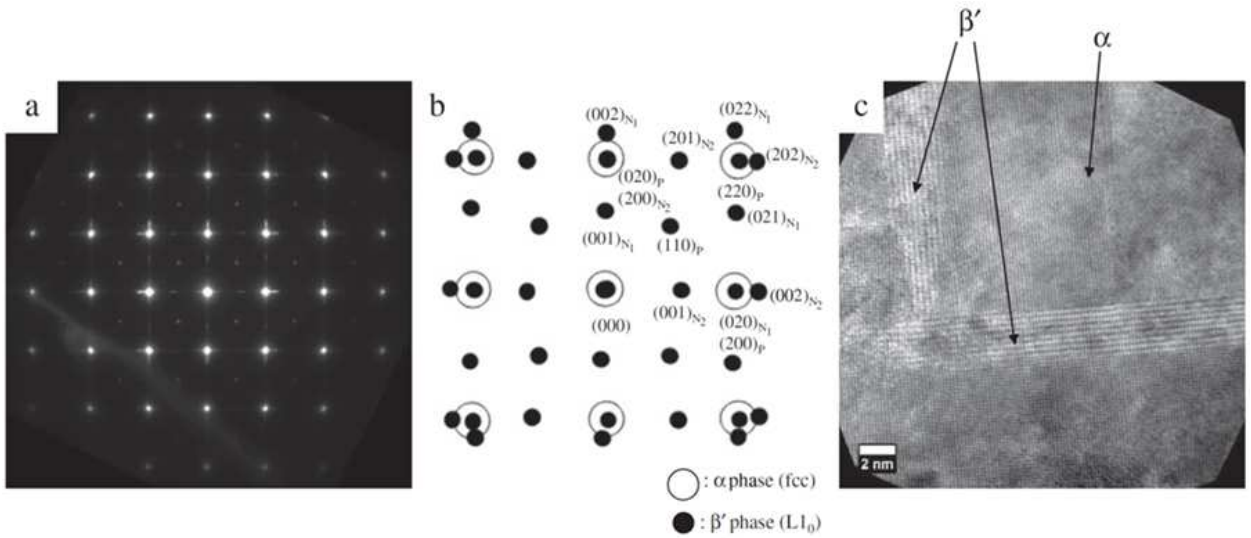
Figure 10. HRTEM micrographs of ST_{1123K}-WQ: (a) a selected area diffraction pattern, (b) a key diagram, and (c) a bright-field image. The beam direction is parallel to [100].

Figure 10 shows the SADP, key diagram, and HRTEM bright field image of ST_{1123K}-WQ [11]. The SADP and the key diagram in Fig. 10 (a) and (b) indicate that the FCC α phase and the three variants of the $L1_0$-type ordered β' phase are superimposed. The $L1_0$-type ordered β' phase is precipitated in the FCC matrix after ST. The streaks on the reflection spots of the $L1_0$-type ordered β' phase indicate that the shape of the β' phase is similar to a thin plate. The HRTEM bright field image in Fig. 10 (c) shows that several nanometer-sized thick plate-shaped β' phase with two variants (N_1, N_2), whose c-axes are normal to the electron beam, are precipitated in the matrix.

It is well known that it is difficult to make a single phase by quenching after high temperature ST; the supersaturated vacancies help the solutes to diffuse more easily and also help to form more clusters, G–P zones, and metastable phases during quenching after high temperature ST. The precipitated β' phase of ST_{1123K}-WQ shown in Fig.9 (d), (e) and Fig. 10 (c) is like a thin plate with a nanometer-scale thickness. These images also suggest that the formation of the β' phase is diffusion controlled. Generally, the formation of precipitates can be considered to be order–disorder transition, diffusionless transformation (martensitic transformation), or diffusional transformation. In the as-solutionized Ag–Pd–Cu–Au alloy used in this case, the dependence of microstructural changes in the precipitated β' phase on both the cooling rate after ST and the ST temperature show that the precipitated $L1_0$-type ordered β' phase is formed during the cooling process and that the growth of the β' phase is influenced by the diffusion process. The hardness increases with an increase in the cooling rate after ST, and consequently, the hardness of ST_{1123K}-WQ increases significantly by quenching after ST (Fig. 6). The fine β' phase in ST_{1123K}-WQ is densely precipitated in the matrix. The hardness of ST_{1123K}-AC increased only slightly, while the hardness of ST_{1123K}-FC decreases, as only coarse β' phases are precipitated in the matrix of ST_{1123K}-AC and ST_{1123K}-FC. Thus, the increase in hardness may be strongly affected by the presence of finely precipitated β' phase. The coherent precipitation of β' phases with long and short axes of around 100 nm and 10 nm, respectively, also occured during ST, although the amount of β' phase decreases with an increase in the ST time. The effect of solid solution hardening in the α, α_1, and α_2 phases is lower than that exerted by the precipitation hardening due to β' phases.

3.1.2. Hardening behavior of Ag–20Pd–12Au–14.5Cu alloy fabricated by liquid rapid solidification

An Ag–20Pd–14.5Cu–12Au alloy with a single α phase can be fabricated using a liquid rapid solidification (LRS) method that employs a melting mechanism, as shown schematically in Fig. 11 [12]. The critical temperature for the order–disorder transformation in the Cu–Pd binary phase diagram is below 1023 K, and hence, at 1023 K, the Cu-rich phase α_1 and Ag-rich phase α_2 decompose, as shown in the Ag–Cu binary phase diagram. Figure 12 shows TEM micrographs of an Ag–20Pd–14.5Cu–12Au alloy fabricated by the LRS method [13]. No precipitation is observed in the matrix.

As shown in Fig. 12 (b) and (c), the LRS alloy consists of a single α phase with face centered cubic structure (FCC). The tensile properties of the as-received Ag–20Pd–14.5Cu–12Au alloy (AS), AS subjected to ST at 1123 K for 3.6 ks in vacuum ($ST_{AS/3.6\,ks}$), LRS alloy (LRS), and LRS alloy subjected to ST at 1123 K for 3.6 ks in vacuum ($ST_{LRS/3.6\,ks}$) are shown in Fig. 13 [13]. The
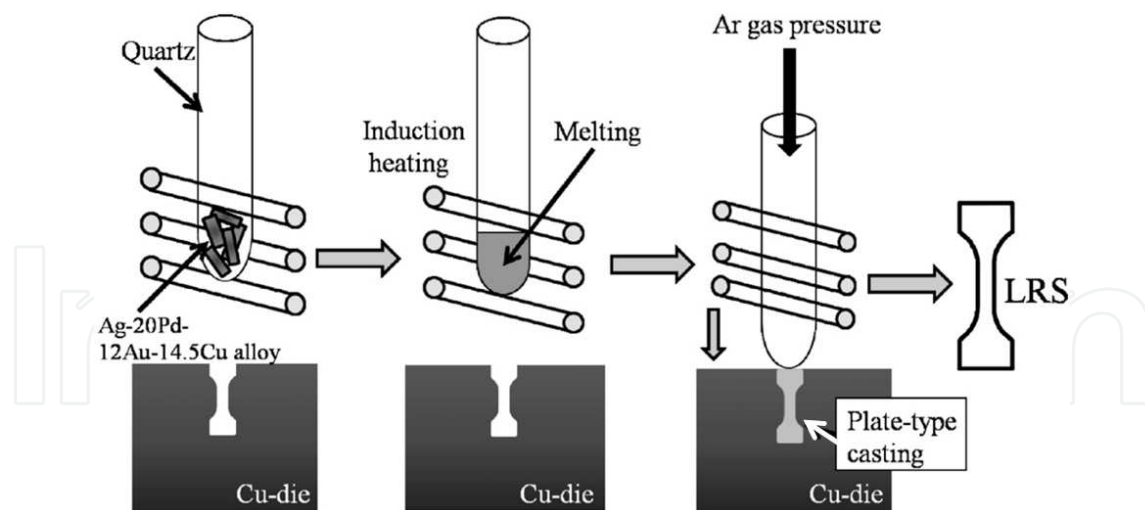
Figure 11. Schematic drawing of LRS method.

tensile strength and 0.2% proof stress of the AS alloy drastically increased after ST. The elongation of AS subjected to ST is smaller than that of the AS alloy. On the other hand, the tensile strength and 0.2% proof stress of the LRS alloy decrease after ST. The reduction in strain and the coarsening of the α phase during ST result in the decrease in the tensile strength and 0.2% proof stress and the increase in elongation. The tensile strength of the LRS alloy and solutionized LRS are relatively smaller than those of the AS alloy and the AS alloy subjected to the ST.
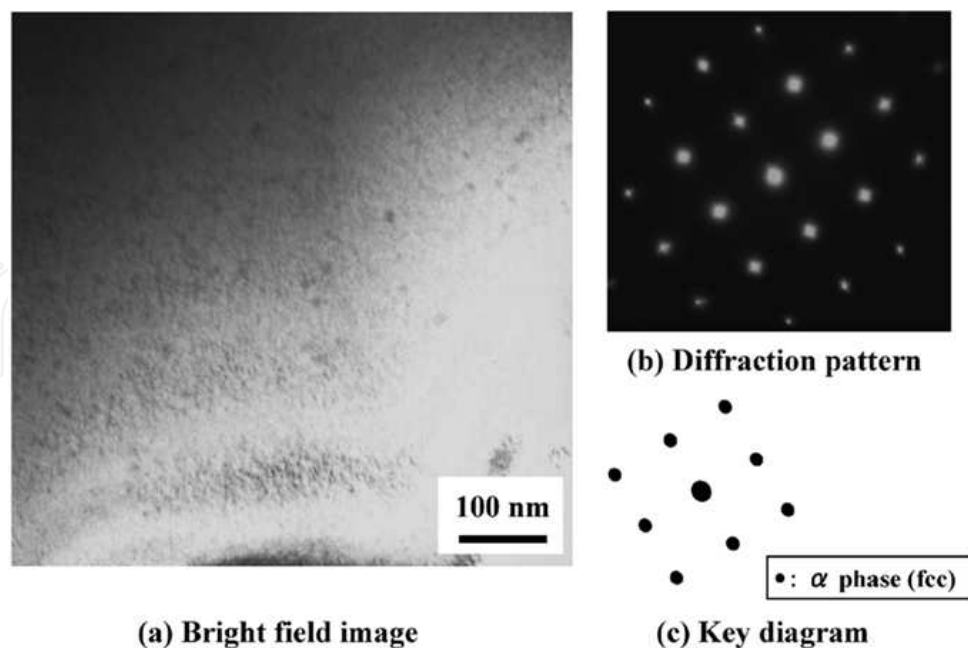
Figure 12. TEM micrographs of alloy fabricated by LRS: (a) bright field image, (b) diffraction pattern and (c) key diagram. Beam direction is parallel to [100].

Figure 14 shows the XRD profiles of the LRS alloy solutionized at 1173 K for 3.6 ks (1173WQ$_{LRS}$/3.6 ks) and the LRS alloy subjected to AT at 673 K for 1.8–28.8 ks following the ST (673WQ$_{LRS}$/1.8 ks-28.8 ks) [12]. A single α phase is identified in the solutionized LRS alloy, whereas, in the LRS alloy subjected to AT after the ST, α_2 and β phases are observed. The Vickers hardness of the solutionized LRS alloy and the LRS alloy subjected to AT are shown in Fig. 15. The hardness of the LRS alloy subjected to AT increases greatly as compared to that of the solutionized LRS alloy with a single α phase owing to the precipitation of β phase.
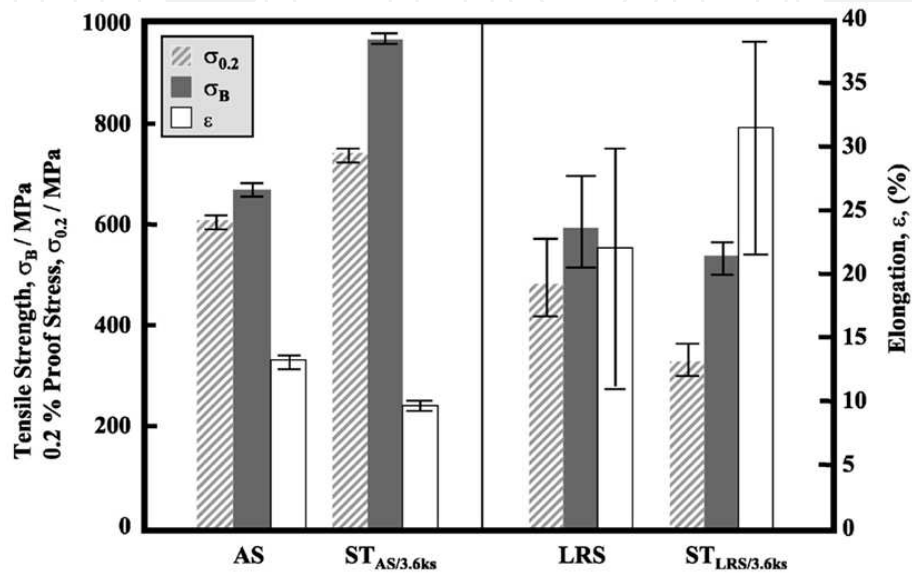

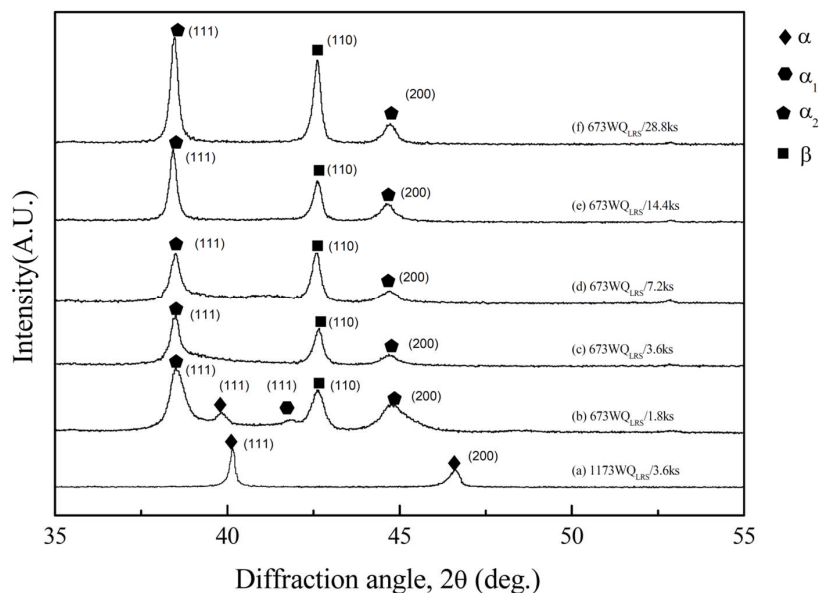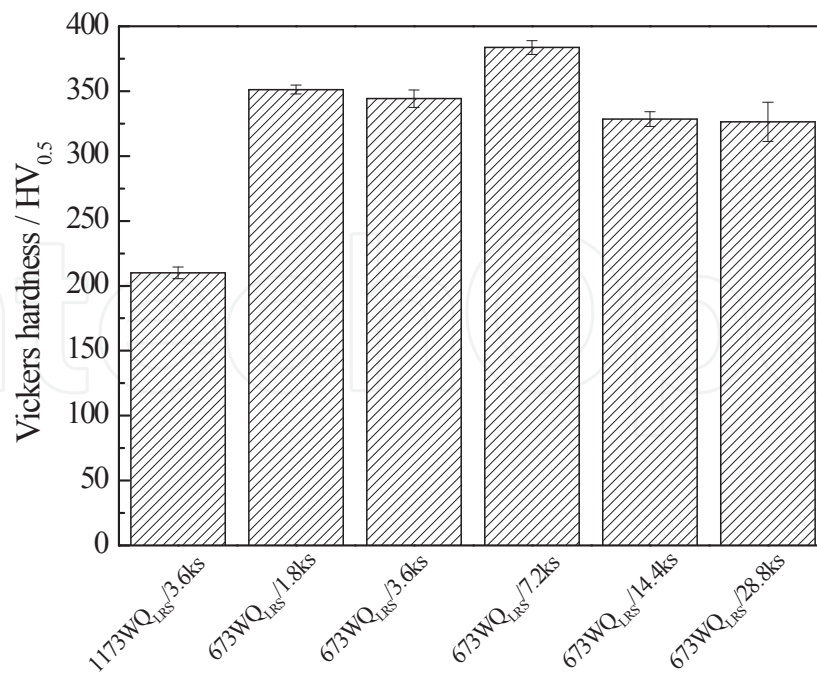**Figure 13.** Tensile properties of AS, ST$_{AS/3.6ks}$, LRS, and ST$_{LRS/3.6ks}$.

Figure 14. XRD profiles of (a) 1173WQ$_{LRS}$/3.6 ks, (b) 673WQ$_{LRS}$/1.8 ks, (c) 673WQ$_{LRS}$/3.6 ks, (d) 673WQ$_{LRS}$/7.2 ks, (e) 673WQ$_{LRS}$/14.4 ks, and (f) 673WQ$_{LRS}$/28.8 ks.

Figure 15. Vickers hardness of $1173WQ_{LRS}$/3.6 ks, $673WQ_{LRS}$/1.8 ks, $673WQ_{LRS}$/3.6 ks, $673WQ_{LRS}$/7.2 ks, $673WQ_{LRS}$/14.4 ks, and $673WQ_{LRS}$/28.8 ks.
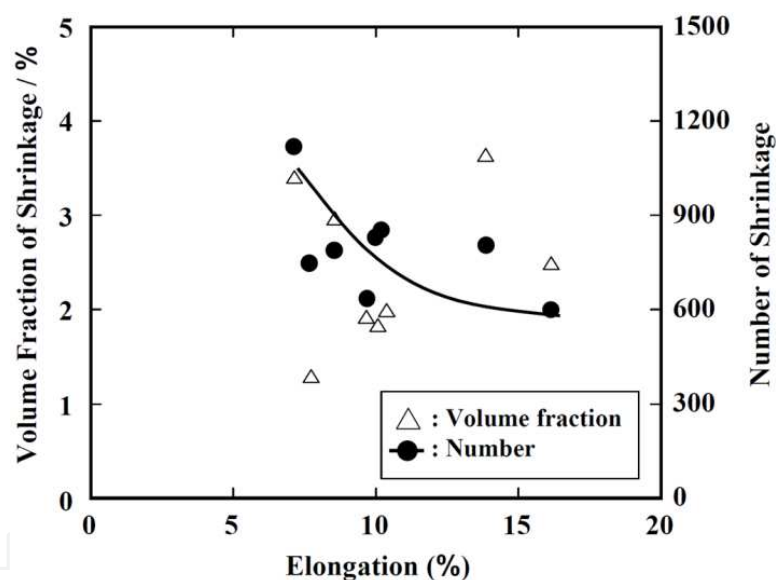
3.2. Fatigue properties

Dental prosthetic products produced by dental casting method are subjected to cyclic stress, i.e., fatigue, because of mastication. Dental castings contain a number of casting defects such as microshrinkages, pores, and surface roughness. The effects of these casting defects on the fatigue properties of cast Ag–20Pd–14.5Cu–12Au alloy were investigated in comparison with the fatigue properties of a drawn Ag–20Pd–14.5Cu–12Au alloy. The tensile properties of the cast specimens and drawn specimens are shown in Fig. 16 [14]. The cast specimens were prepared using a lost wax method. The drawn alloy bars were solutionized at 1073K for 3.6 ks in vacuum and then cooled in air (D-1073AC (drawn)). The heat treatment produced a microstructure with a matrix similar to that in an as-cast alloy. For the mechanical testing, the following specimen dimension were used: gauge diameter 3 mm and gauge length 20 mm for cast specimens, gauge diameter 2 mm and gauge length 20 mm for drawn specimens. The surfaces of the cast specimens for tensile tests were sand blasted (non-polished). The tensile strength and 0.2% proof stress of the cast specimens were higher than those of the drawn specimens. The distribution of the elongation of the cast specimens was larger than that of the elongation of the drawn specimens. The amount of intermetallic β phase that leads to the high strength and low ductility is greater in the cast specimens than in the drawn specimens. The microstructure of the cast specimens may be coarser than that of the drawn specimens. The relationship between the volume fraction and the number of the microshrinkage as measured on the fracture surface of the non-polished cast specimen and the elongation is shown in Fig. 17 [14]. Although no correlation was obtained between the volume fractions of the micro-shrinkage and elongation, the elongation decreases with an increase in the number of the

microshrinkage. The surfaces of some fatigue test specimens were finished by buff-polishing (polished). Drawn specimens with a gauge diameter of 5 mm and a gauge length of 20 mm were used for the fatigue tests. Fatigue tests were carried out in order to obtain an S–N curve for each specimen at a stress ratio, R, of 0.1 and a frequency of 10 Hz with a sine waveform in air at room temperature (295 K). As can be seen in Fig.18 [14], the fatigue strength of the non-polished specimen is similar to that of the polished specimen in both the low-cycle fatigue life region and the high-cycle fatigue life region. The distribution of the fatigue strength of both the cast specimens is greater than that of the fatigue strength of the drawn specimens. The fatigue strength of the non-polished cast specimens was 352–492 MPa ($\Delta\sigma_{max}$ (range of σ_{max}) = 140 MPa) at 10^5 cycles and 209–284 MPa ($\Delta\sigma_{max}$ = 75 MPa) at 10^6 cycles. The fatigue strength of the polished cast specimens was 347–565 MPa ($\Delta\sigma_{max}$ = 218 MPa) at 10^5 cycles and 233–251 MPa ($\Delta\sigma_{max}$ = 18 MPa) at 10^6 cycles. The fatigue strength of both cast specimens was lower than that of the drawn specimens, and is extremely low in the high-cycle fatigue life region, where N_f exceeds 10^5 cycles. The fatigue limits, which represent the fatigue strength for which the number of cycles to failure is over 10^7 cycles, are around 210 MPa. On the other hand, although the fatigue limit of the drawn specimen was not obtained, it is expected to be near 400 MPa. Figure 19 [14] shows SEM fractographs taken near the site at which fatigue crack initiated in the cast specimens and the drawn specimen, which then broke in the high-cycle fatigue life region. In the case of the drawn specimen, the fatigue crack initiates at the slip band on the specimen surface, but in the case of the cast specimens, the fatigue crack initiates from the microshrinkage near the specimen surface. In general, slip damage accumulates on the specimen surface, after which extrusion and intrusion take place. Next, the stress concentration occurs and a fatigue crack initiates along the slip plane. If there are polishing scars, defects, etc. on the specimen surface, stress concentration occurs, and the fatigue strength becomes lower. The sizes of the microshrinkage areas and pores whose size exceeds 10 μm were measured, because the microshrinkage areas and pores whose size is less than 10 μm were difficult to distinguish from dimples on the fracture surface in the measurement on the fractographs. The number and size of the microshrinkage, whose size exceeds 10 μm as measured on the fatigue fracture surface, are greater than those measured on the cross-section near the fatigue fracture surface. Therefore, the fatigue crack propagates by preferentially linking the areas of microshrinkage. The number and size of the pores measured on the fatigue fracture surface is nearly equal to those measured on the cross-section near the fatigue fracture surface. Therefore, the effect of the pores on the fatigue properties is much smaller than that of the microshrinkage.

In general, dental prosthetic materials sustain a stress of 20–230MPa during mastication. Moreover, they must be able to sustain such cyclic stress over 10,000,000 times (10^7 cycles), which is the calculated number of cycles that is equivalent to the number of times food will be chewed in a span of ten years. Therefore, the target value of the fatigue limit of the cast specimen is considered to be 230MPa, which is the greatest mastication stress. Since the fatigue strength of this cast specimen is strongly dependent on the size of the microshrinkage that acts as the fatigue crack initiation site, it is prudent to estimate the size of the microshrinkage. It is also beneficial to know the size that can be tolerated, in order to achieve reliability in casting that is subjected to fatigue fracture.
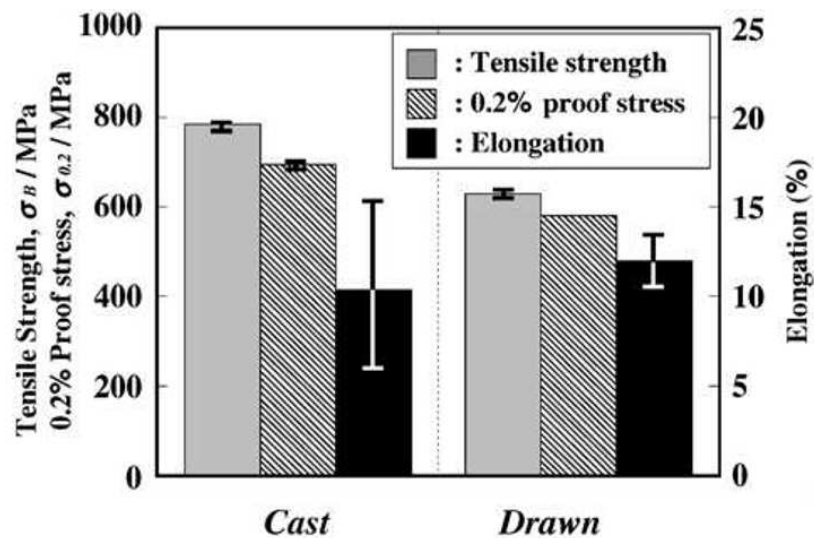
Figure 16. Tensile properties of non-polished cast specimens (Cast) and drawn specimens (Drawn: D-1073AC (drawn)).


Figure 17. Relationships between volume fraction or number of shrinkage on fractograph and elongation of non-polished cast specimen.

3.3. Fretting–fatigue properties

Fretting–fatigue properties are also important for alloys that are used for dental applications, because during mastication, fretting occurs between the alloys and the teeth opposite them. Fig. 20 [15] shows the S–N curves of AS alloys subjected to ST at 1123 K for 3.6 ks followed by WQ and AT at 673 K for 1.8 ks followed by WQ that were obtained from plain fatigue and fretting–fatigue tests. The fretting–fatigue strength of the Ag–20Pd–14.5Cu–12Au alloy subjected to ST and AT decreases significantly as compared to the fatigue strength without fretting (plain–fatigue strength). The fretting–fatigue strength after the ST decreases by
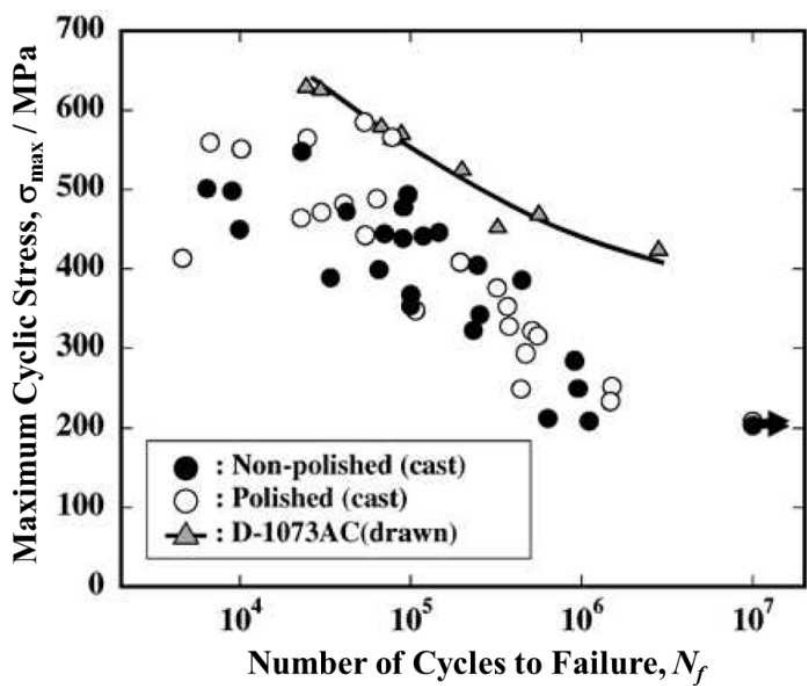
Figure 18. S-N_f curves of non-polished cast specimen (Non-polished (cast)), polished cast specimen (Polished (cast)), and drawn specimen (D-1073AC(drawn)).

σ_{max} = 250MPa
N_f = 9.50 × 10^5

σ_{max} = 233MPa
N_f = 1.48 × 10^6

σ_{max} = 496MPa
N_f = 2.89 × 10^6
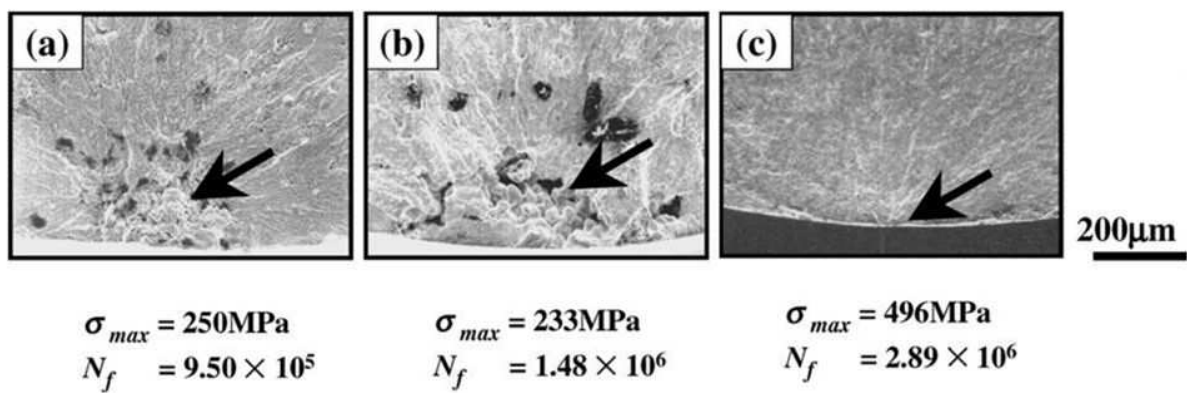
Figure 19. SEM fractographs in high-cycle fatigue life region: (a) non-polished cast specimen, (b) polished cast specimen, and (c) drawn specimen. Arrows indicate crack initiation sites. σ_{max} and N_f are the maximum cyclic stress and number of cycles to failure, respectively.

approximately 13% in the low-cycle fatigue life region and by approximately 40% in the high-cycle fatigue life region, as compared to the fatigue strength of the solutionized alloy. Moreover, the fretting–fatigue strength after the AT decreases by approximately 60% as compared to that after the ST, especially in the high-cycle fatigue life region. A schematic drawing of crack initiation from fretting damage region is shown in Fig.21 [15]. Although a slip between the specimen and a fretting pat does not occur in the stick region, a microslip between the specimen and the fretting pat occurs in the slip region during the deformation of the specimen. A significant stress concentration is generated by the damage to the specimen surface caused

by the microslip. Fracture morphologies caused by crack initiation and propagation then appear. It can be observed that several traces of fretting wear are distributed in the slip region of both materials. These wear traces are generated by the accumulation of wear debris on the fretting pad or on the fretting–fatigue specimen. These traces of fretting wear are distributed more closely in the slip region of the material that was subjected to AT. Therefore, the fatigue life decreases significantly because the fretting–fatigue crack initiation life and the propagation life decrease in the material that was subjected to AT.
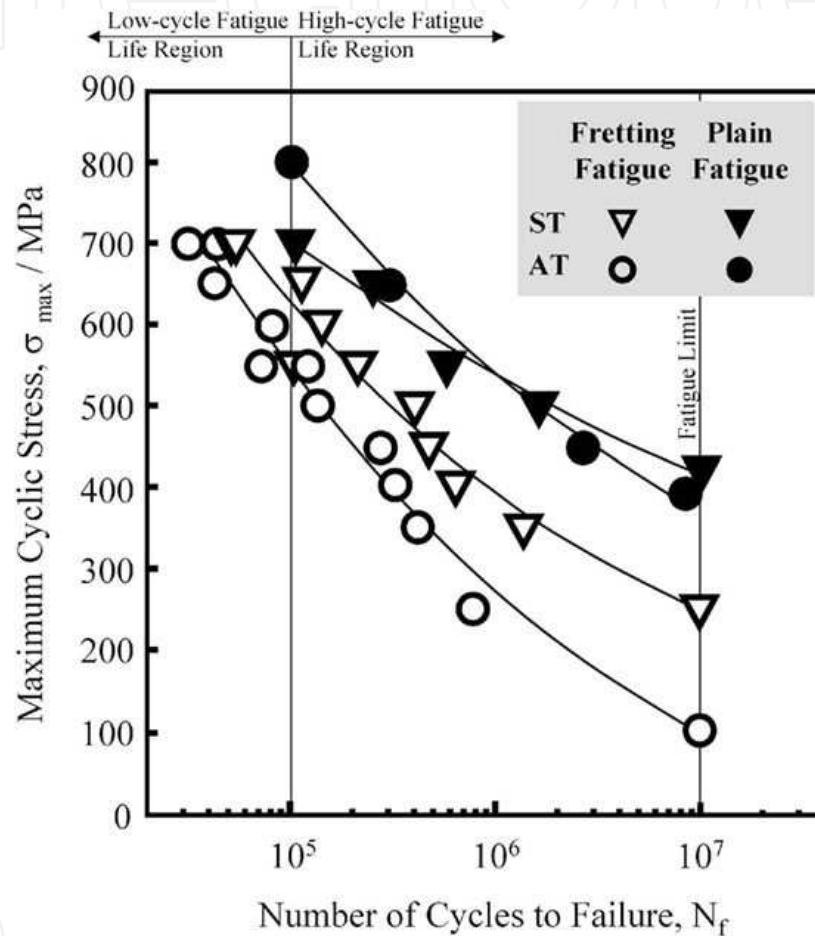
Figure 20. S–N curves of Ag–20Pd–14.5Cu–12Au alloy subjected to ST and AT obtained from plain fatigue and fretting fatigue tests.

### 3.4. Friction wear properties of Ag–20Pd–12Au–14.5Cu alloy in corrosive environments

Mastication also leads to friction wear in dental alloys and in teeth. As the friction wear progresses, this eventually causes problems with mastication. Therefore, the evaluation of the friction wear properties of dental alloys is quite important to the health of the teeth and oral cavity. The friction wear property of Ag–20Pd–14.5Cu–12Au alloy that was subjected to various heat treatments was evaluated in three corrosive environments: distilled water, 0.9% NaCl solution, and 3% NaCl solution. In the friction wear testing, the alloys were subjected to
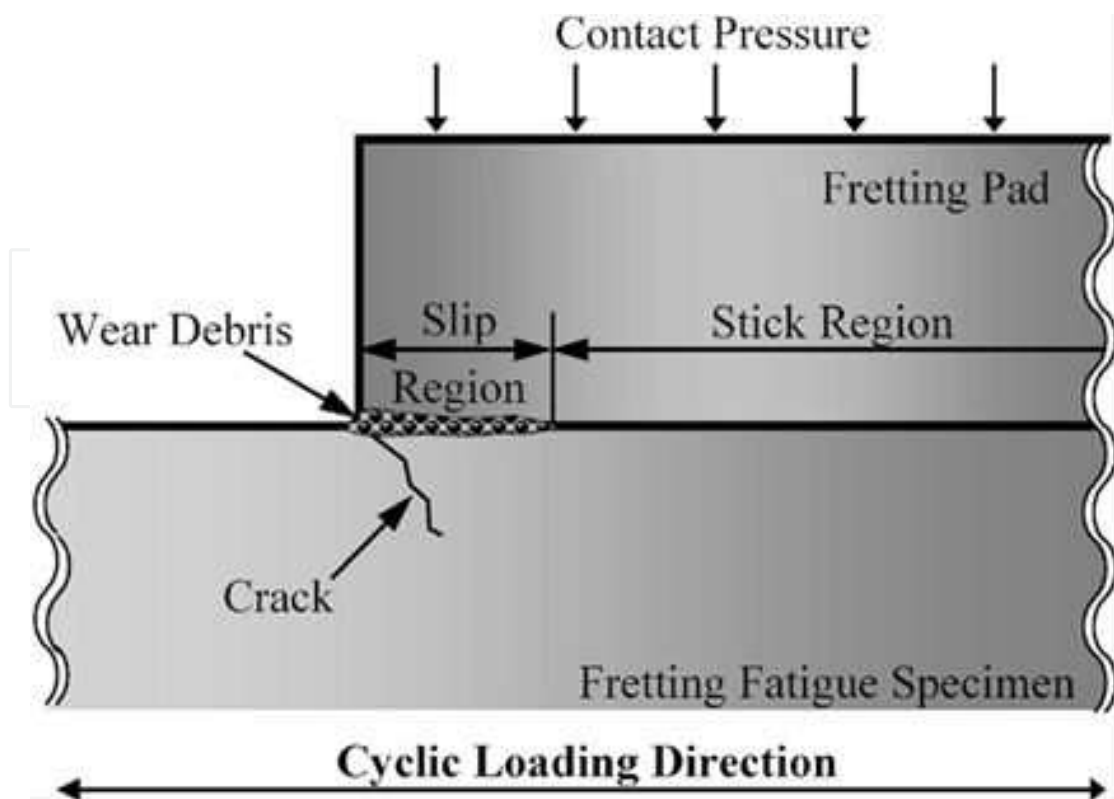
Figure 21. Schematic drawing of crack initiation from fretting damage region.

STs at 1073 and 1123 K subjected to WQ, AT at 673 K, and ST at 1073 K subjected to AC. It was found that the friction wear properties are influenced by the microstructures of this alloy as well as by the corrosive environments. The friction wear tests were performed using a pin-on-disk-type friction wear tester. The applied load, sliding diameter, sliding velocity, sliding distance, and test duration were 9.8 N, 3 mm, 31.4 mm/s (100 rpm), 4.71×10^5 mm, and 115 ks, respectively. The temperature of all the solutions was 310 K. The weight loss was calculated by subtracting the combined weight of a specimen and the mating material it after the friction wear test, from their combined weight before the test. Figure 22 [16] shows the total weight loss and wear surface roughness of specimens that were subjected to each heat treatment in each corrosive solution. The total weight loss (the sum of the weight losses of the specimen and the material opposite it) of the specimens was largest in distilled water, 0.9% NaCl and then 3% NaCl solution. A pin with a diameter of 1 mm, which was made from the as-received alloy, was used as the mating material. The weight losses of the specimens and the mating materials increased with a decrease in the kinematic viscosity of the solutions, due to the increase in the average friction coefficient during the friction wear tests. In every environment, the total weight loss of the specimen subjected to AT at 673 K, which gives a large amount of precipitated β phase, was small compared with that of the other heat-treated specimens, due to the higher degree of hardness near the contact surface, as also shown in Fig.4 [10]. The total weight loss increased with the surface roughness of the contact surface. The hardness near the contact surface changed the surface roughness of the contact surface. The mode of wear of these alloys in a corrosive environment is adhesive wear. No tarnish, which is corrosion caused

by chloride ion and the production of silver chloride coatings were found on the wear marks or wear particles after the friction wear tests in each environment.
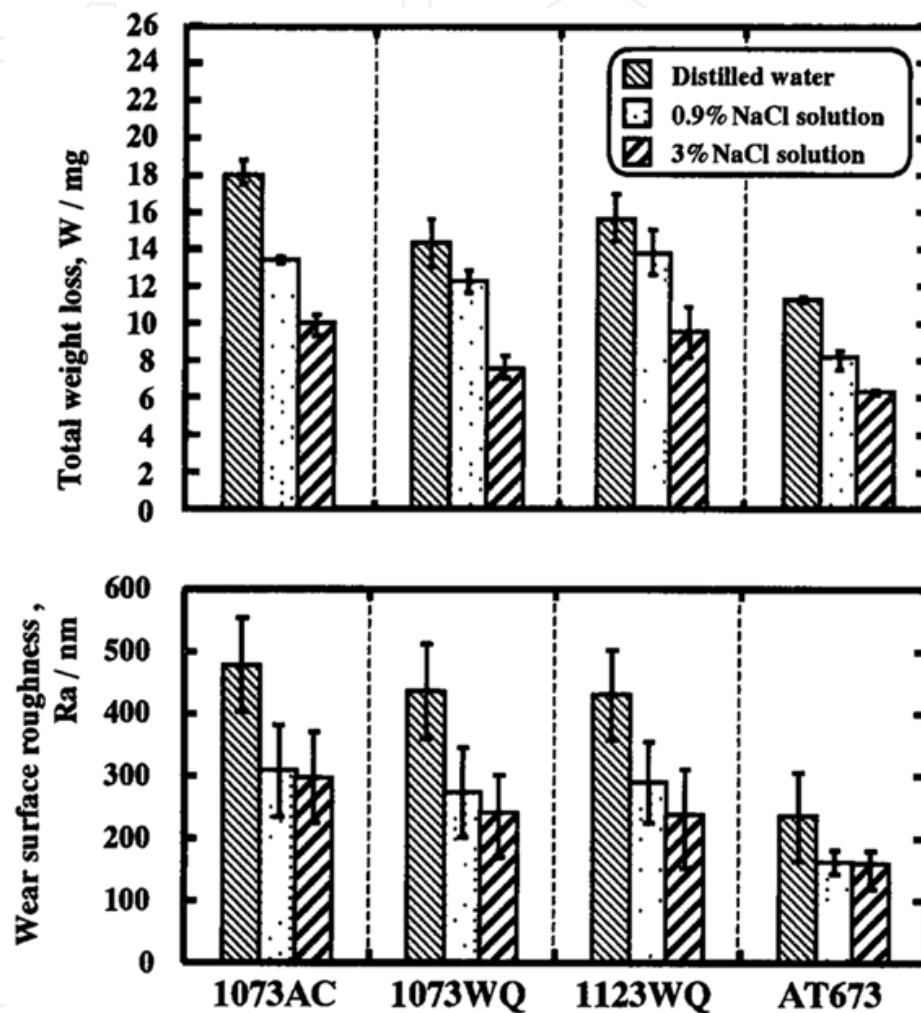
Figure 22. Total weight loss and wear surface roughness of specimen subjected to each heat treatment in each corrosive solution. 1073AC, 1073WQ, 1123WQ, and AT673 indicate specimens subjected to ST at 1073 K for 3.6 ks followed by AC or WQ, ST at 1123 K for 3.6 ks followed by WQ and AT at 673 K for 1.8 ks.

3.5. Corrosion properties

The study of the corrosion properties of dental alloys is very important due to their usage in severe oral environments. The formation of corrosion compounds on the surface causes the alloy to tarnish. The corrosion behaviors of commercial Ag-22.41Pd-15.64Cu-12.1Au alloys in various solutions were investigated by Ichinose [17]. The alloy was casted into a plate with 2 mm in thickness by heating at 973 K for 30 min. Table 2 [17] shows the rest-potential of the as-cast alloy in 1% NaCl solution, artificial saliva, human saliva, and 1% $C_3H_6O_3$ solution. The

rest-potentials in 1% NaCl solution and 1% $C_3H_6O_3$ solution show obviously higher values than those for artificial and human saliva. The organic compounds in the artificial and human saliva inhibit the redox reaction by adsorbing on the surface of the alloy or by the formation of complexes with the metal. AgCl was formed on the surface of the alloy after anode polarization sweeping up to 1800 mV in 1% NaCl solution, artificial saliva, and human saliva, which contain Cl ion. 90% of the released ions of the as-cast alloy immersed in human saliva for 24 h were Cu ions (Fig.23 [17]). Cu contributes to the enhancement the hardness of the alloy. However, a large amount of Cu in the alloy decreases the corrosion resistance. The as-cast alloy was subjected to a softening treatment at 1073 K for 3 min followed by WQ (softened). An ingot of the commercial Ag-22.41Pd-15.64Cu-12.1Au alloy was subjected to ST at 1123 K for 2 h and then heated at 723 K for 1 h or 20 h (723 K 1h aged and 723 K 20 h aged, respectively). As shown in Fig. 24 [17], the amounts of released Cu and Ag ions depend on the heat treatment that the alloy is subjected to, because the corrosion behavior is influenced by the microstructure of the alloy. The amount of Cu ions released from the as-cast alloy is higher than that released from heat-treated alloys. Cavities formed by shrinkage during casting in the as-cast alloy are the reason for this phenomenon.

| Solution	Rest–potential
1% NaCl solution	112.7 ± 22.4 mV
Artificial saliva	24.7 ± 17.2 mV
Human saliva	28.0 ± 20.4 V
1% $C_3H_6O_3$ solution	113.6 ± 37.7 mV

Table 2. Rest-potential of as-cast Ag-22.41Pd-15.64Cu-12.10Au alloy in various corrosive solutions.
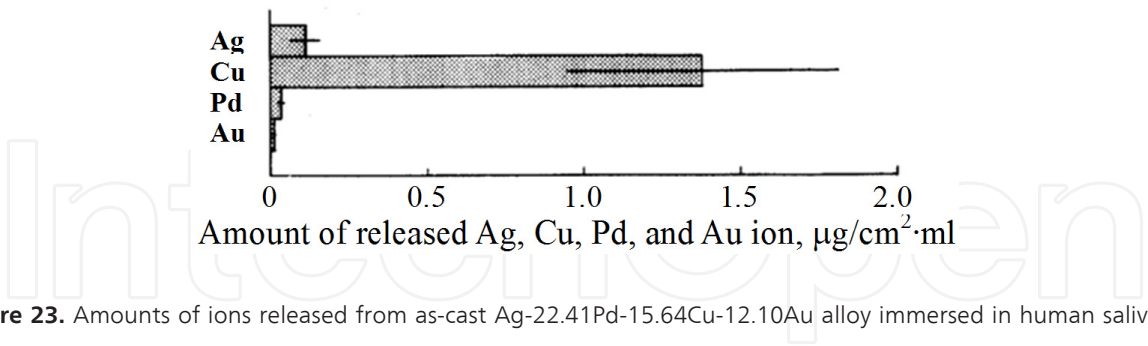
Figure 23. Amounts of ions released from as-cast Ag-22.41Pd-15.64Cu-12.10Au alloy immersed in human saliva for 24 h.

4. Summary

This chapter details the microstructure, the mechanical properties (hardness, fatigue, fretting-fatigue, and friction-wear), and the corrosion properties of the Ag–Pd–Cu–Au alloys, especially the Au-20Pd-14.5Cu-12Au alloy. Most studies on these alloys have been carried out in Japan and Korea. Although other dental materials such as high carat gold alloys, amalgam,
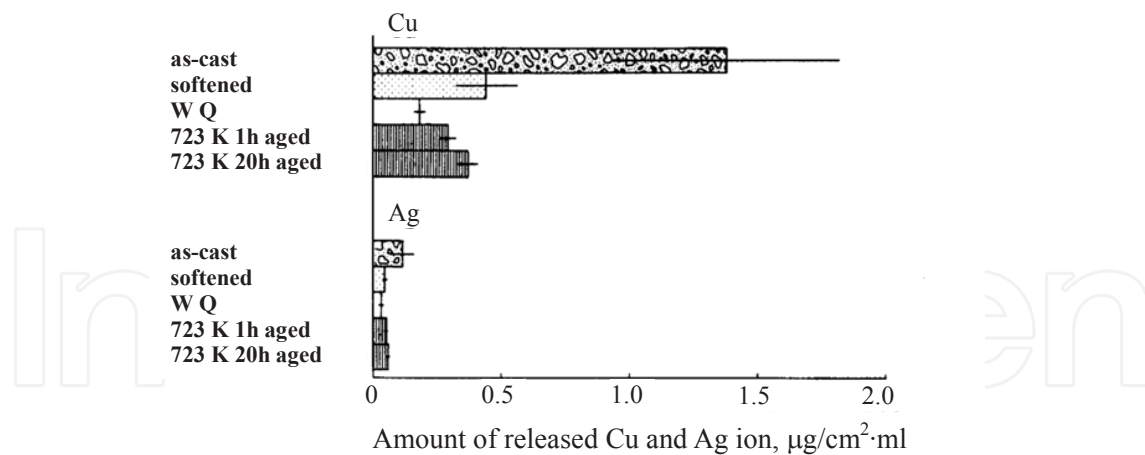
Figure 24. Cu and Ag release amounts from as-cast, softened, WQ, 723 K 1h aged, and 723 K 20 h aged Ag-22.41Pd-15.64Cu-12.10Au alloys immersed in human saliva for 24 h.

and non-precious alloys such as titanium and its alloys, cobalt-chromium alloys, and nickel–chromium alloys are also important, the authors intended to introduce present results of studies on the Ag–Pd–Cu–Au alloys to researchers who study dental materials all over the world through this chapter.

A variety of test results showed that the hardness of the alloy can be drastically increased through ST at a temperature over 1073 K subjected to WQ. The L1$_0$-type ordered phase (β' phase) precipitated during the quenching process leads to this unique hardening behavior. The hardness of the alloy increased with an increase in the cooling rate following ST, because the size of the β' phase decreased and the number of the β' phase increased with an increase in the cooling rate following ST.

It was also found that the fatigue strength of a cast alloy was considerably less than that of a drawn alloy. The fatigue crack of a cast alloy initiated preferentially at the shrinkage near the specimen surface. The deviation of the fatigue strength of the cast alloy became small by relating the fatigue life to the maximum stress intensity factor that was calculated, assuming that the shrinkage that begins as a fatigue crack initiation site becomes an initial crack. This means that the size of the shrinkage strongly affects the fatigue strength of this cast alloy. A tolerable shrinkage size that satisfies the target value of the fatigue limit (230 MPa) of this cast alloy was calculated to be below 80 μm, using a derived equation that describes the relationship between the maximum stress intensity factor and the number of the cycles to failure.

The fretting–fatigue strength of the Ag–20Pd–12Au–14.5Cu alloy subjected to ST and aging treatment decreased significantly as compared to the fatigue strength without fretting. The fretting–fatigue strength after the aging treatment decreased by approximately 60% as compared to that following the ST, especially in the high-cycle fatigue life region.

The total weight losses (the sum of the weight losses of a specimen and of the mating material) of specimens were largest in distilled water, subjected to 0.9% NaCl and then 3% NaCl solution. In every environment, the total weight loss of a specimen subjected to aging treatment at 673

K, which gives a large amount of precipitated β phase, was small compared with that of the other heat treated specimens, due to the higher degree of hardness near the contact surface.

The Ag-Pd-Cu-Au alloys have excellent mechanical and corrosion properties, but the relatively high cost and supplied amounts of these alloys are issues to be used widely. The authors hope that the Ag-Pd-Cu-Au alloys is further investigated by many researchers for its wide usage.

Acknowledgements

Author details

Junko Hieda, Mitsuo Niinomi, Masaaki Nakai and Ken Cho

Department of Biomaterials Science, Institute for Materials Research, Tohoku University, Katahira, Aoba-ku, Sendai, Japan

References

[1] Ohta M, Shiraishi T, Yamane M. Phase transformation and age-hardening of Au-Cu-Pd ternary alloys. Journal of Materials Science 1986;21(2) 529-535.

[2] Winn H, Tanaka Y, Shiraishi T, Udoh K, Miura E, Hernandez RI, Takuma Y, Hisatsune K. Two types of checkerboard-like microstructures in Au–Cu–Pd ternary alloys. Journal of Alloys and Compounds 2000;306(1-2) 262-269.

[3] Seol HJ, Son KH, Yu CH, Kwon YH, Kim HI. Precipitation hardening of a Cu-free Au–Ag–Pd–In dental alloy. Journal of Alloys and Compounds 2005;402(1-2) 130-135.

[4] Seol HJ, Shiraishi T, Tanaka Y, Miura E, Hisatsune K, Kim HI. Ordering behaviors and age-hardening in experimental AuCu–Zn pseudobinary alloys for dental applications Biomaterials 2002;23(24) 4873-4879.

[5] Hisatsune K, Sakrana A, Hamasaki K, Hernandez R, Salonga JP. Phase transformation in a dental gold alloy for soldering. Journal of Alloys and Compounds 1997;261(1-2) 308-312.

[6] Lee JH, Yi SJ, Seol HJ, Kwon YH, Lee JB, Kim HI. Age-hardening by metastable phases in an experimental Au–Ag–Cu–Pd alloy. Journal of Alloys and Compounds 2006;425(1-2) 210-215.

[7] Santos ML, Acciari HA, Vercik LCO, Guastaldi AC. Laser weld: microstructure and corrosion study of Ag–Pd–Au–Cu alloy of the dental application. Materials Letters 2003;57(13-14) 1888-1893.

[8] Seol HJ, Kim GC, Son KH, Kwon YH, Kim HI. Hardening mechanism of an Ag–Pd–Cu–Au dental casting alloy, Journal of Alloys and Compounds 2005;387(1-2) 139-146.

[9] Fukui H, Shinoda S, Mukai M, Yasue K, Hasegawa J. Effect of heat treatment on mechanical properties of type IV gold and 12wt% Au-Pd-Ag alloys. The Japanese Society for Dental Materials and Devices 1992;11(1) 141-148.

[10] Fukui H, Mukai M, Shinoda S, Hasegawa J. Strengthening mechanism of Au-Pd-Ag-Cu system. The Japanese Society for Dental Materials and Devices 1993;12(6) 685-690.

[11] Kim YH, Niinomi M, Hieda J, Nakai M, Fukui H. Formation of L10-type ordered β' phase in as-solutionized dental Ag–Pd–Au–Cu alloys and hardening behavior. Materials Science and Engineering: C 2012;32(3) 503–509.

[12] Kim YH, Niinomi M, Nakai M, Akahori T, Kanno T, Fukui H. Mechanism of unique hardening of dental Ag–Pd–Au–Cu alloys in relation with constitutional phases. Journal of Alloys and Compounds 2012;519 15–24.

[13] Akahori T, Niinomi M, Nakai M, Tsutsumi H, Kanno T, Kim YH, Fukui H. Relationship between unique hardening behavior and microstructure of dental silver alloy subjected to solution treatment. Journal of the Japan Institute of Metals 2010;74(6) 337-344.

[14] Mizumoto T, Niinomi M, Nakano Y, Akahori T, Fukui H. Fatigue properties of cast Ag-Pd-Cu-Au-Zn alloy for dental applications in the relation with casting defects. Materials Transactions 2002;43(12) 3160-3166.

[15] Akahori T, Niinomi M, Nakai M, Kawagishi W, Fukui H, Fretting-fatigue properties and fracture mechanism of semi-precious alloy for dental applications. Journal of The Japan Institute of Metals 2008;72(1) 63-71.

[16] Mizumoto T, Niinomi M, Akahori T, Katou K, Fukui H. Friction wear properties of dental Ag-Pd-Cu-Au alloy in corrosive environments. The Japanese Society for Dental Materials and Devices 2003; 22(6) 459-468.

[17] Ichinose S. Corrosion behavior of dental Au-Pd-Cu-Au alloy in various solutions. The Japanese Society for Dental Materials and Devices 1992;11(1) 149-168.

[18] Seol HJ, Lee DH, Lee HK, Takada Y, Okuno O, Kwon YH, Kim HI. Age-hardening and related phase transformation in an experimental Ag–Cu–Pd–Au alloy. Journal of Alloys and Compounds 2006;407(1-2) 182-187.

[19] Yu CH, Park MG, Kwon YH, Seol HJ, Kim HI. Phase transformation and microstructural changes during ageing process of an Ag-Pd-Cu-Au Alloy. Journal of Alloys and Compounds 2008;460(1-2) 331-336.

[20] Kanzawa Y, Uzuka T, Kondo, Shoji M. Study on the Ag-Pd alloy. Journal of the Japan Society for Dental Apparatus and Materials 1963;4 157-160.

[21] Yasuda K. Study on the age-hardeability of dental precious metal alloys. Journal of the Japan Society for Dental Apparatus and Materials 1969;10 156-166.

[22] Ohta M, Hisatsune K, Yamane M. Study on the age-hardenable silver alloy. Journal of the Japan Society for Dental Apparatus and Materials 1975;16 144-149.

[23] Ohta M, Hisatsune K, Yamane M. Age Hardening of Ag-Pd-Cu dental alloy. Journal of the Less-Common Metals 1979;65(1) 11-21.

[24] Ohta M, Shiraishi T, Hisatsune K, Yamane M. Age-hardening of dental Ag-Pd-Cu-Au alloys. Journal of Dental Research 1980;59(11) 1966-1971.

[25] Tanaka Y, Miura E, Shiraishi T, Hisatsune K. Nano-precipitates generated in the dental silver–palladium–gold alloy. Materia Japan 2004;12 1036.

[26] Tanaka Y, Seol HJ, Ogata T, Miura E, Shiraishi T, Hisatsune K. Hardening mechanism of dental casting gold-silver-palladium alloy by higher-temperature heat-treatment. The Japanese Society for Dental Materials and Devices 2003;22 (2) 69.